



Title	A novel approach for vegetation classification using UAV-based hyperspectral imaging
Author(s)	Ishida, Tetsuro; Kurihara, Junichi; Angelico Viray, Fra; Baes Namuco, Shielo; Paringit, Enrico C.; Jane Perez, Gay; Takahashi, Yukihiro; Joseph Marciano, Joel, Jr.
Citation	Computers and electronics in agriculture, 144, 80-85 <a href="https://doi.org/10.1016/j.compag.2017.11.027">https://doi.org/10.1016/j.compag.2017.11.027</a>
Issue Date	2018-01
Doc URL	<a href="http://hdl.handle.net/2115/76656">http://hdl.handle.net/2115/76656</a>
Rights(URL)	<a href="https://creativecommons.org/licenses/by-nc-nd/4.0/">https://creativecommons.org/licenses/by-nc-nd/4.0/</a>
Type	article (author version)
File Information	draft_paper_v15_with_figre1_6.pdf



[Instructions for use](#)

1 **A novel approach for vegetation classification using UAV-based**  
2 **hyperspectral imaging**

3  
4 **Tetsuro Ishida<sup>a,\*</sup>, Junichi Kurihara<sup>a</sup>, Fra Angelico Viray<sup>b</sup>, Shiho Baes**  
5 **Namuco<sup>c</sup>, Enrico C. Paringit<sup>b</sup>, Gay Jane Perez<sup>c</sup>, Yukihiro Takahashi<sup>a</sup>, Joel**  
6 **Joseph Marciano, Jr.<sup>d</sup>**

7 <sup>a</sup>Faculty of Science, Hokkaido University, Sapporo, Japan

8 <sup>b</sup>Training Center for Applied Geodesy and Photogrammetry, University of the  
9 Philippines Diliman, Quezon City, Philippines

10 <sup>c</sup>Institute of Environmental Science and Meteorology, University of the  
11 Philippines Diliman, Quezon City, Philippines

12 <sup>d</sup>Advanced Science and Technology Institute, Department of Science and  
13 Technology, Quezon City, Philippines

14  
15 *\*Correspondence to:* T. Ishida, Faculty of Science, Hokkaido University, Kita 10  
16 Nishi 8, Kita-ku, Sapporo, Hokkaido 060-0810, Japan.  
17 (ishida.tetsuro@sci.hokudai.ac.jp)

18

19 **Abstract**

20 The use of unmanned aerial vehicle (UAV)-based spectral imaging offers  
21 considerable advantages in high-resolution remote-sensing applications.  
22 However, the number of sensors mountable on a UAV is limited, and selecting  
23 the optimal combination of spectral bands is complex but crucial for conventional  
24 UAV-based multispectral imaging systems. To overcome these limitations, we  
25 adopted a liquid crystal tunable filter (LCTF), which can transmit selected  
26 wavelengths without the need to exchange optical filters. For calibration and  
27 validation of the LCTF-based hyperspectral imaging system, a field campaign  
28 was conducted in the Philippines during March 28–April 3, 2016. In this  
29 campaign, UAV-based hyperspectral imaging was performed in several  
30 vegetated areas, and the spectral reflectances of 14 different ground objects  
31 were measured. Additionally, the machine learning (ML) approach using a  
32 support vector machine (SVM) model was applied to the obtained dataset, and a  
33 high-resolution classification map was then produced from the aerial  
34 hyperspectral images. The results clearly showed that a large amount of  
35 misclassification occurred in shaded areas due to the difference in spectral  
36 reflectance between sunlit and shaded areas. It was also found that the

37 classification accuracy was drastically improved by training the SVM model with  
38 both sunlit and shaded spectral data. As a result, we achieved a classification  
39 accuracy of 94.5% in vegetated areas.

40

DRAFT

41 **Keywords**

42 ● Liquid crystal tunable filter

43 ● Unmanned aerial vehicle

44 ● Vegetation classification

45 ● Machine learning

46

DRAFT

47 **1. Introduction**

48 Spectral reflectance data collected from vegetated areas can provide very  
49 valuable information on factors such as the presence or absence of certain tree  
50 species, plant growth stages, and plant diseases. The relationships between  
51 plant properties and spectral reflectance data have been studied using different  
52 types of spectroscopic sensors (e.g., Schmidt and Skidmore, 2003; Kuska et al.,  
53 2015). Recently, unmanned aerial vehicle (UAV) technology, which is evolving  
54 rapidly, has been applied to survey systems for precision agriculture, and UAVs  
55 equipped with spectral sensors have been tested in agricultural applications by  
56 many studies. For example, Garcia-Ruiz et al. (2013) conducted a UAV-based  
57 aerial survey with multispectral cameras over a citrus orchard, and found that  
58 UAV-based datasets yielded better classification accuracy than aircraft-based  
59 datasets for diseased citrus trees. Moreover, Peña et al. (2013, 2015) applied  
60 UAV-based multispectral imaging for the early detection of weed seedlings in  
61 combination with object-based image analysis.

62 Previous UAV-based spectral imaging systems mostly used multiple imaging  
63 sensors with independent optics and different band pass filters to obtain simple  
64 vegetation indices such as the normalized difference vegetation index (NDVI).

65 However, because the number of mountable imaging sensors is limited by the  
66 payload weight capacity of the UAV, it is difficult to obtain in-depth spectral  
67 information using this type of multispectral imaging system. Hence, we adopted  
68 a liquid crystal tunable filter (LCTF) for a UAV-based hyperspectral imaging  
69 system. The LCTF is an optical band pass filter whose center wavelength is  
70 electrically tunable. Because of the flexibility of spectral bands, hyperspectral  
71 imaging with LCTF technology is applicable to a wide variety of remote-sensing  
72 applications. This technology was first put into practical use on a space-borne  
73 instrument by Hokkaido University, and it has already been mounted on several  
74 microsattellites developed by Tohoku University and Hokkaido University (e.g.,  
75 Sakamoto et al., 2015). More recently, the Philippines' first microsattelite,  
76 DIWATA-1, was built by scientists and engineers from the Philippines, Hokkaido  
77 University, and Tohoku University under the PHL-Microsat Program. DIWATA-1  
78 contains a space-borne multispectral imager (SMI) that employs LCTF  
79 technology. For calibration and validation of SMI imagery, a field campaign with  
80 the UAV-based hyperspectral imaging system using LCTF technology was  
81 conducted in the Philippines.

82 Advanced spectral imaging systems on UAVs can achieve highly efficient data

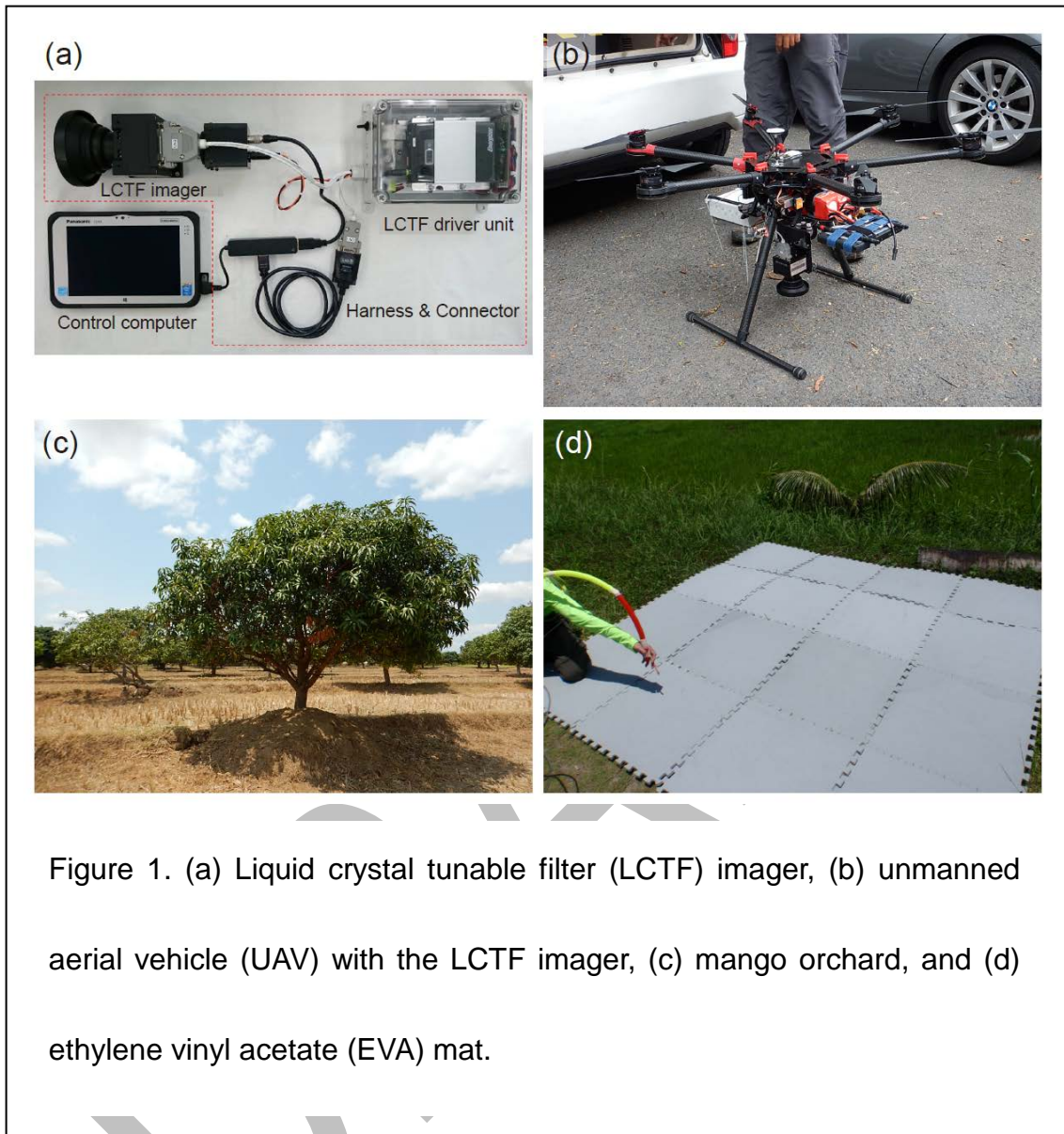
83 acquisition. However, large amounts of complex vegetation information are  
84 gathered on a daily basis, and this data can be difficult to process using  
85 conventional processing techniques. Recently, machine learning (ML) has  
86 become one of the most powerful approaches for examining such complex  
87 datasets (so-called big data). In general, ML is a data analysis method that can  
88 be used to discover underlying structures, similarities, or dissimilarities present  
89 in big data. In the case of supervised learning, the ML model is trained by user  
90 inputs so that it gains experience throughout the training process. The ML is  
91 widely applicable for identification, detection, classification, quantification,  
92 estimation, and prediction in precision agriculture (Singh et al., 2016).

93 The UAV-based hyperspectral imaging system described in this study can  
94 realize aerial images with a resolution on the order of tens of millimeters. Thus, it  
95 could be useful for leaf-scale plant disease detection when combined with the  
96 ML approach. Therefore, this new survey platform using LCTF technology will  
97 make a significant contribution to future precision agriculture research. In this  
98 paper, we present a UAV-based high-resolution vegetation classification map,  
99 and evaluate the validity of this new platform.

100

101 **2. Observations**

102 The field campaign was conducted in Gerona and Ramos, Tarlac, the  
103 Philippines, during March 28–April 3, 2016. In this campaign, UAV-based  
104 hyperspectral imaging was carried out in several vegetated areas under clear  
105 sky conditions. Each operation was conducted for 10 min because the maximum  
106 flight time of the UAV is only approximately 20 min due to the payload weight.  
107 Figure 1(a) shows the hyperspectral imager with LCTF technology (hereafter  
108 referred to as the LCTF imager) and related devices used in the field campaign.  
109 The LCTF imager can capture two-dimensional hyperspectral images ranging  
110 from 460 to 780 nm at 1 nm intervals (321 bands in total), and the full width at  
111 the half maximum of the spectral band ranges from 5 nm (at 460 nm) to 25 nm  
112 (at 780 nm). The maximum switching time of the spectral bands is 300 ms, and  
113 the exposure time of the imager typically ranges from 5 to 50 ms, depending on  
114 the reflectance of the ground object and the solar zenith angle. The capture time  
115 of a single image is approximately 1 s, which includes the switching time,  
116 exposure time, and data processing time. Figure 1(b) shows the rotating



117

118 wing UAV (DJI's Matrice 600 Hexacopter) with the LCTF imager. In this field

119 campaign, LCTF-based hyperspectral images of ground objects were recurrently

120 captured from 460 to 780 nm at 10 nm intervals, which equates to 33 images per

121 cycle. Approximately 2,000 images were acquired in all. The flight height was set

122 to 25 m or 50 m in order to capture the target objects at either leaf- or

123 canopy-scales. The image resolution was 656 pixels × 494 pixels, and the  
124 expected ground sampling distance (GSD) was approximately 57 mm at a height  
125 of 25 m, and 115 mm at a height of 50 m. The study area was a mango orchard  
126 located in Gerona City (15°34'N, 120°32'E), which mainly contains mango trees,  
127 dried grass, and soil (see Figure 1(c)). In the field campaign, we placed white  
128 sacks on the ground as landmarks. In proximal sensing, diffuse reflectance  
129 standards are often used as the reference for solar irradiance to obtain the  
130 spectral reflectance of a ground object. As the size of typical reflectance  
131 standards is small compared with the resolution of the imager, we utilized a mat  
132 made of ethylene vinyl acetate (EVA) as a substitute for the reflectance  
133 standards in this field campaign (see Figure 1(d)). The deployed EVA mat  
134 measured 2.4 m × 2.4 m, and its reflectance was independently measured in  
135 advance. Using the reflectance of the EVA mat, the spectral reflectance of a  
136 target object on the same image at a wavelength of  $\lambda$ ,  $R_{obj(\lambda)}$ , can be given by  
137 the following equation:

$$R_{obj(\lambda)} = \frac{L_{obj(\lambda)}}{L_{eva(\lambda)}} \cdot R_{eva(\lambda)}$$

138 where  $L_{obj(\lambda)}$  and  $L_{eva(\lambda)}$  are the measured spectral radiance of the target  
139 object and the EVA mat, respectively, and  $R_{eva(\lambda)}$  is the reflectance of the EVA

140 mat. Note that the spectral reflectances measured by the LCTF imager in this  
141 study were calculated using this equation.

142

### 143 **3. Data processing**

144 Spectroscopic imaging using a conventional hyperspectral sensor employs  
145 push-broom line scanning; therefore, the technique is generally combined with a  
146 moving platform such as an aircraft or an Earth-observation satellite (e.g., Shaw  
147 and Burke, 2003). Hence, accurate GPS measurements and complicated post  
148 data processing methods such as georeferencing are necessary to construct  
149 so-called spectral data cubes (e.g., Suomalainen et al., 2014). This remains  
150 difficult for most users when handling hyperspectral data; thus, simpler  
151 approaches should be developed to facilitate the use of hyperspectral data. To  
152 address this issue, we developed a snapshot hyperspectral imaging system that  
153 does not require accurate global positioning system (GPS) measurements so  
154 that the acquired dataset can be processed by a simple image processing  
155 technique, detailed below.

156 In the case of aerial snapshot hyperspectral imaging by the LCTF imager, the  
157 captured area shifts slightly from image to image, which is due to small attitude

158 perturbations of the UAV. In order to obtain a spectral data cube, it is necessary  
159 to precisely overlap the time-sequential hyperspectral images using an image  
160 processing technique. In this study, we applied Speeded-Up Robust Features  
161 (SURF), which is an algorithm that extracts so-called SURF descriptors (in other  
162 words, unique features) from images (e.g., Bay et al., 2008). The SURF  
163 descriptors are in the form of 64-element vectors that express the local gradation  
164 of images. Thus, the features of an image are assumed to be reflected in the  
165 SURF descriptors. The similarity of images is quantified by comparing SURF  
166 descriptors. Figure 2 shows an example of feature matching results

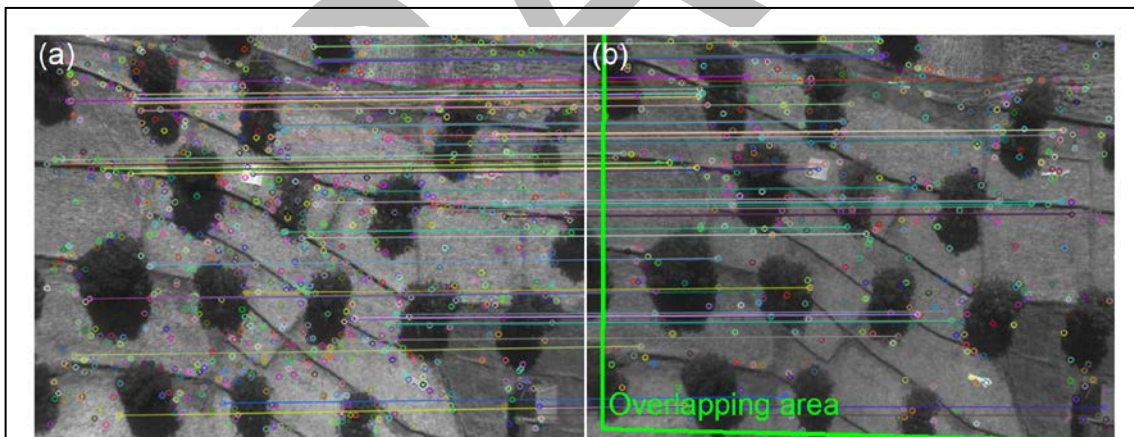


Figure 2. Example of feature matching results for two time-sequential hyperspectral images at (a) 680 nm and (b) 690 nm. The color-coded circles indicate the extracted features. Similar features are associated with color-coded lines between the images.

167

168 applied to two time-sequential hyperspectral images taken at (a) 680 nm and (b)  
169 690 nm. The color-coded circles indicate the extracted SURF descriptors, and  
170 similar features are associated with color-coded lines between the images.  
171 Based on the associated pixel locations, a matrix is produced for geometric

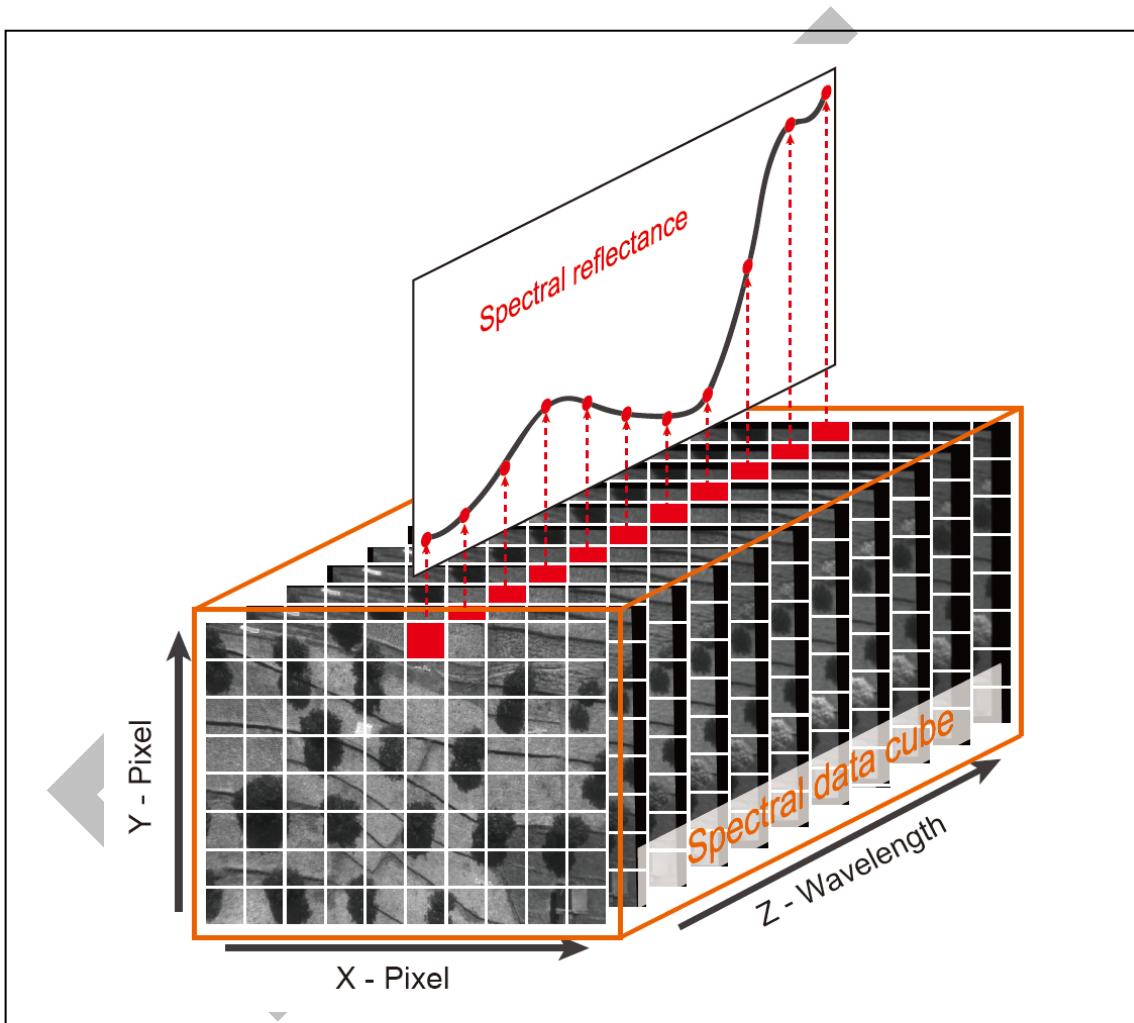


Figure 3. Structure of the spectral data cube. In the field campaign, the LCTF imager recurrently captured spectral images ranging from 460 to 780 nm at 10 nm intervals, which equates to 33 images per cycle.

172

173 image transformation from one image to another. The area surrounded by green  
174 lines in Figure 2(b) is the overlapping area calculated by the transformation  
175 matrix. In total, 32 repetitions of the overlapping process from the 460-nm image  
176 to the 780-nm image were used to produce a spectral data cube, as illustrated in  
177 Figure 3. In the spectral data cube, the spectral reflectance of a captured object  
178 can be obtained from each pixel location along the z-axis. With this image  
179 processing technique, the spectral reflectances of 14 different ground objects  
180 were extracted from the aerial hyperspectral images. Figure 4 shows the mean  
181 spectral reflectance of the captured objects. The numbers in parentheses  
182 indicate the number of extracted spectral reflectances used for each mean  
183 spectrum. The error bars indicate the standard deviation. The figure omits the  
184 error bar of the “man-made objects” category for the sake of a better  
185 visualization. This is because the mean spectral reflectance of the man-made  
186 objects was produced by averaging the spectral reflectances of different types of  
187 objects such as rooftops and sacks, and the standard deviation was very large  
188 (up to 0.24) compared to the others. It is well known that the spectral reflectance  
189 in a shaded area is quite different from that in a sunlit area (e.g., Zhang et al.,  
190 2015; Hsieh et al., 2016); therefore, we chose only sunlit areas for

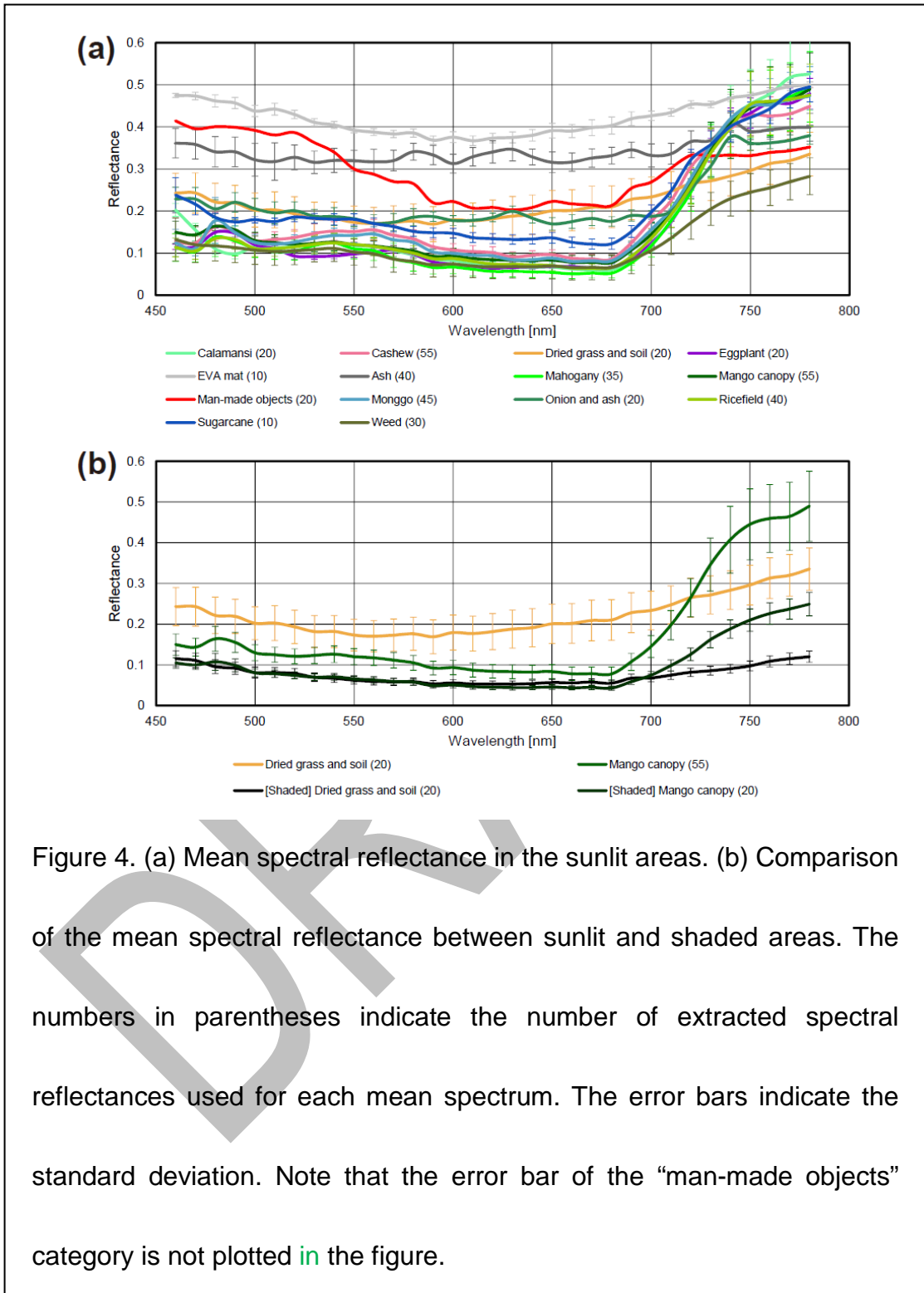


Figure 4. (a) Mean spectral reflectance in the sunlit areas. (b) Comparison of the mean spectral reflectance between sunlit and shaded areas. The numbers in parentheses indicate the number of extracted spectral reflectances used for each mean spectrum. The error bars indicate the standard deviation. Note that the error bar of the “man-made objects” category is not plotted in the figure.

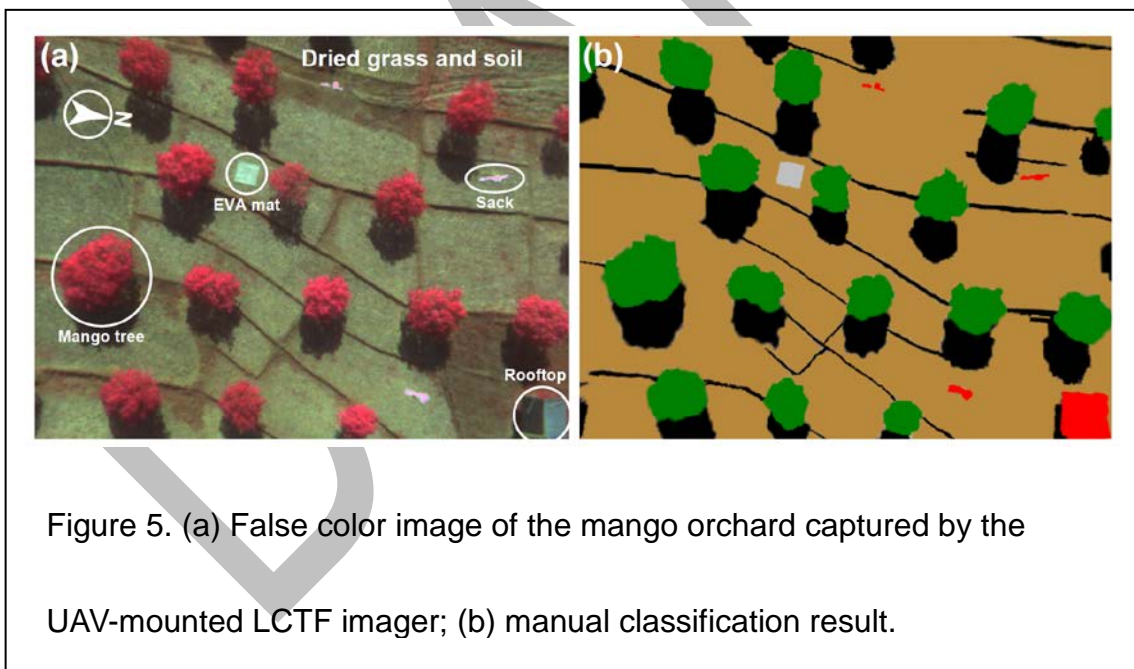
191

192 extracting the mean spectra in Figure 4(a).

193

194 **4. Results and discussion**

195 Using a support vector machine (SVM), which is one type of supervised ML  
196 model, we classified the spectral reflectances obtained by the image processing  
197 technique described in Section 3, and created a high-resolution classification  
198 map of the study area. Figure 5(a) shows a false color image of the study area  
199 observed by the LCTF imager, and consists of hyperspectral images taken at  
200 550 nm, 650 nm, and 780 nm, which represent green, red, and near-infrared  
201 channels, respectively. These three bands were selected to emphasize

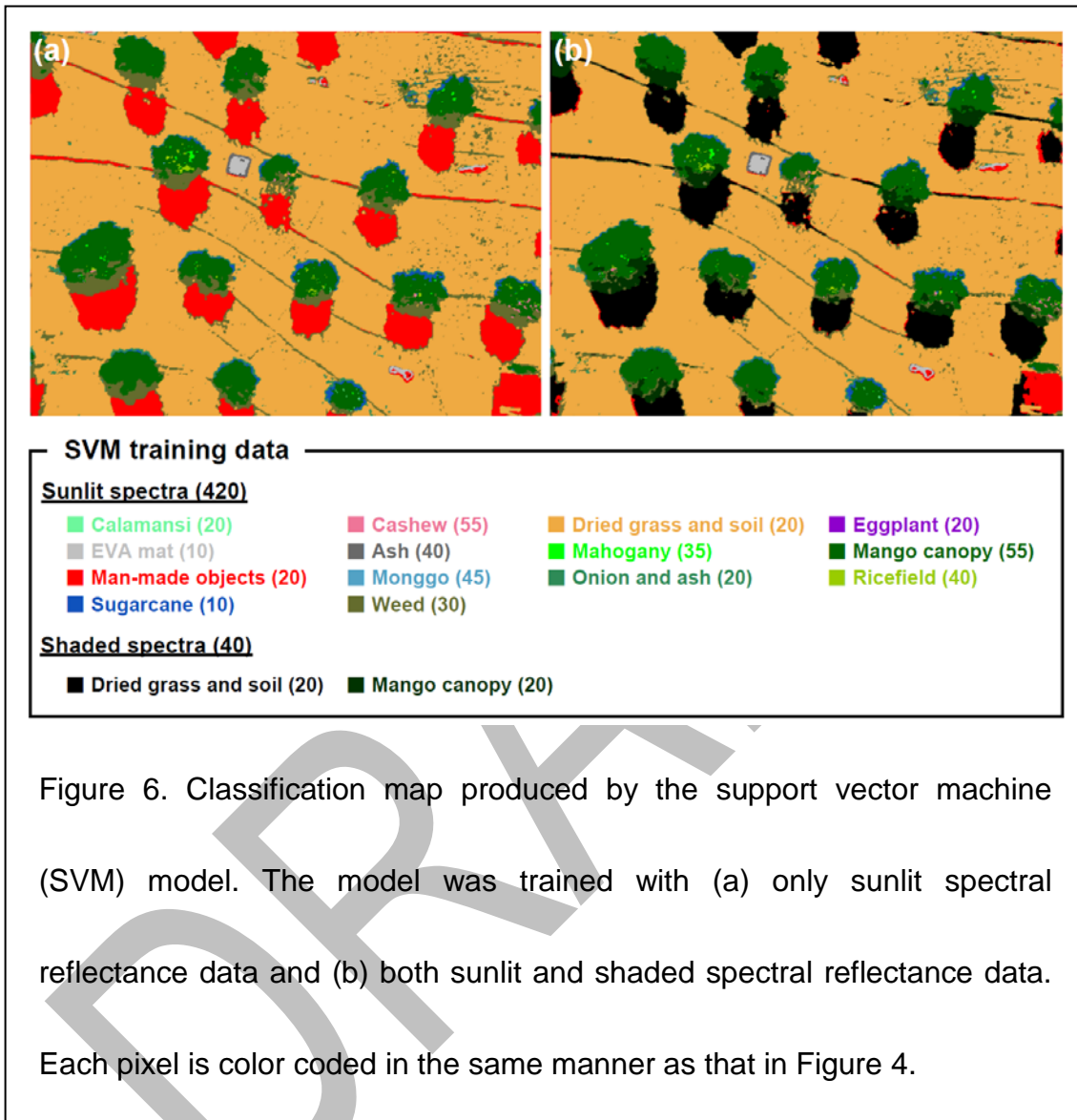


202 the vegetation in red color. Images were taken at an altitude of 50 m at 15:23  
203 PHT on March 29, 2016, when the sun was located in the west with a solar  
204 zenith angle of 50.69°. Therefore, the ground under the mango trees was largely  
205

206 shaded. Based on this figure, we manually classified each individual pixel (see  
207 Figure 5(b)). Although the manual classification result could contain some  
208 mistakes, the ground objects were categorized into the following approximate  
209 object categories: (1) mango canopy, (2) dried grass and soil, (3) shaded dried  
210 grass and soil, (4) man-made objects, and (5) the EVA mat. For comparison with  
211 the classification results obtained by the SVM model, we used Figure 5(b) to  
212 elucidate the correct classification according to the discussion below.

213 Figure 6(a) shows the classification map produced by the SVM model, which  
214 was trained with the 420 sunlit spectral reflectance data presented in Figure 4(a).  
215 During the training phase, we used 33-bands of each spectral reflectance as  
216 33-dimensional information, and mapped the data onto a 33-dimensional  
217 hyperplane using the SVM model. The shape of the decision boundary, which is  
218 the determining factor of a classification, can be mapped by the SVM model  
219 based on the selected kernel type, the kernel parameters, and the training  
220 dataset. Therefore, a proper setting and training dataset should be selected to  
221 classify the data at a certain high level (e.g., Huang et al., 2002). In this study,  
222 the radial basis function (RBF) kernel was selected, and the cost parameter  $C$   
223 and the gamma  $\gamma$  of the RBF kernel were tuned to 312 and 0.5, respectively, in

224 order to minimize the cross-validation estimate of the test set error.



225

226 As mentioned above, Figure 5(b) shows the results of a manually defined

227 classification for comparison with the classification map produced by the SVM.

228 Accordingly, each classified pixel in Figure 6(a) was compared with the defined

229 category in Figure 5(b), and the classification accuracy was calculated by

230 dividing the number of correctly classified pixels by the total number of pixels. As

231 a result, the classification accuracy was 81.0%, owing to the large amount of  
232 misclassification in shaded areas. Image pixels located in the shaded mango  
233 canopy and shaded dried grass and soil areas were misclassified as weeds and  
234 man-made objects, respectively. Thus, classification accuracy is highly  
235 dependent on the coverage of shaded areas in cases where the spectral images  
236 have a high resolution, and where sunlit and shaded areas can be distinguished  
237 by the data. Early studies discriminated shaded pixels from non-shaded pixels  
238 by using shadow masking, and the pixel data were processed separately to  
239 achieve high classification accuracy (e.g., Roussel et al., 2016; Qiao et al., 2017).  
240 In this study, however, shaded and non-shaded pixel data were processed by a  
241 common data processing method without shadow masking. In Figure 4(b), the  
242 spectral reflectances of the mango canopy and dried grass and soil in sunlit and  
243 shaded areas are compared. There was a clear difference between spectral  
244 reflectances of the mango canopy and dried grass and soil in shaded areas, as  
245 well as between those in sunlit areas. This means that sunlit and shaded  
246 spectral reflectances can be classified together in a single process. Therefore,  
247 we modified the SVM model by training it simultaneously with both sunlit and  
248 shaded spectral data. Figure 6(b) shows the classification map produced by the

249 modified training dataset. The classification accuracy increased to 94.5%; that is,  
250 it was improved by 13.5% from that of Figure 6(a). Thus, this result clearly  
251 indicates the importance of using shaded spectra for the training process of the  
252 SVM model.

253 It should be noted that there were still some misclassifications around the  
254 boundaries between different objects. Because the structure of flexible objects  
255 such as mango canopies is continuously slightly deformed by the wind, its  
256 appearance could be different in each image. This small change in appearance  
257 leads to feature matching errors; consequently, some non-overlapping regions  
258 are created between the transformed images. Hence, the challenge for future  
259 research will be to minimize such non-overlapping regions by reducing the  
260 feature matching errors. The LCTF imager at present takes ~1 s to acquire a  
261 single image, but acquisition time can be shortened by approximately half by  
262 upgrading the current system. Therefore, it is expected that misclassifications  
263 derived from feature matching errors can be reduced in the near future.

264

## 265 **5. Conclusion**

266 Whereas most hyperspectral sensors adopt push-broom line scanning, the

267 LCTF imager utilizes a snapshot imaging system. This advantage allows users  
268 to handle the hyperspectral data more easily and obtain science products more  
269 rapidly using a simple image processing technique. With this method, we were  
270 able to precisely overlap time-sequential hyperspectral images through image  
271 processing using SURF descriptors, and the spectral reflectances of 14 different  
272 ground objects were successfully extracted. Additionally, the SVM model trained  
273 with spectral reflectances was used for vegetation classification, and a  
274 high-resolution classification map produced from the aerial hyperspectral images  
275 was presented.

276 Originally, the SVM model trained with only sunlit spectral data was applied to  
277 the mango orchard, but the resulting classification map contained a large  
278 number of misclassifications in shaded areas. This was because spectral  
279 reflectances in shaded areas deviated from those in sunlit areas. Thus, we  
280 trained the SVM model using both sunlit and shaded spectral reflectances, and  
281 applied the updated model to the study area. As a result, we achieved a  
282 classification accuracy of 94.5%, which represents a 13.5% improvement on  
283 results produced using only sunlit spectral reflectance data. Thus, the results  
284 clearly indicate that this new survey platform using the LCTF imager is useful for

285 vegetation classification, and has the potential to make valuable contributions to  
286 precision agriculture. Nevertheless, a statistical study is necessary in future work  
287 to verify the robustness of the proposed method, because the classification  
288 accuracy was estimated from a single event in this study. The results also  
289 revealed some misclassification areas around the boundaries between different  
290 objects. This was caused by feature matching errors that resulted in the creation  
291 of some non-overlapping regions between transformed images. The  
292 classification accuracy can be further improved by decreasing the feature  
293 matching errors in future research.

## 295 **Acknowledgements**

296 The Philippine field campaign was conducted as part of the PHL-Microsat  
297 Program, which was financially supported by the Philippine Council for Industry,  
298 Energy and Emerging Technology Research and Development of the  
299 Department of Science and Technology (PCIEERD-DOST). The PHL-Microsat  
300 Program is a Philippine government program that aims to build, launch, and  
301 utilize microsatellite technology for disaster monitoring and natural resource  
302 management. The program was built by PCIEERD-DOST, University of the

303 Philippines Diliman, Hokkaido University, and Tohoku University. The authors  
304 are indebted to Phil-Lidar 1 and PHL-Microsat Projects 4 and 5 team members  
305 for providing valuable assistance during this field campaign. Open Source  
306 Computer Vision Library (OpenCV), which is an open source computer vision  
307 and machine learning software library, was utilized in this study.

308

## 309 **References**

310 Bay, H., Ess, A., Tuytelaars, T., Van Gool, L., 2008. Speeded-Up Robust  
311 Features (SURF). *Comput. Vis. and Image Underst.* 110 (3), 346–359.

312 Garcia-Ruiz, F., Sankaran, S., Maja, J.M., Lee, W.S., Rasmussen, J., Ehsani, R.,  
313 2013. Comparison of two aerial imaging platforms for identification of  
314 Huanglongbing-infected citrus trees. *Comput. Electron. Agric.* 91, 106–115.

315 Hsieh, Y.T., Wu, S.T., Chen, C.T., Chen, J.C., 2016. Analyzing spectral  
316 characteristics of shadow area from ASD-40 high radiometric resolution  
317 aerial images. *Int. Archives Photogramm., Remote Sens. Spatial Inform. Sci.*  
318 *XLI-B7*, 223–227.

319 Huang, C., Davis, L.S., Townshend, J.R., 2002. An assessment of support vector  
320 machines for land cover classification. *Int. J. Remote Sens.* 23 (4), 725–749.

321 Kuska, M., Wahabzada, M., Leucker, M., Dehne, H.W., Kersting, K., Oerke, E.C.,  
322 Steiner, U., Mahlein, A.K., 2015. Hyperspectral phenotyping on microscopic  
323 scale: towards automated characterization of plant-pathogen interactions.  
324 *Plant Methods* 11 (28), 1-14.

325 Peña, J.M., Torres-Sánchez, J., de Castro, A.I., Kelly, M., López-Granados, F.,  
326 2013. Weed mapping in early-season maize fields using object-based  
327 analysis of unmanned aerial vehicle (UAV) images. *PLoS ONE* 8 (10), 1–11.

328 Peña, J.M., Torres-Sánchez, J., Serrano-Pérez, A., de Castro, A.I., Kelly, M.,  
329 López-Granados, F., 2015. Quantifying efficacy and limits of unmanned  
330 aerial vehicle (UAV) technology for weed seedling detection as affected by  
331 sensor resolution. *Sensors* 15 (3), 5609–5626.

332 Qiao, X., Yuan, D., Li, H., 2017. Urban shadow detection and classification using  
333 hyperspectral image. *Journal of the Indian Society of Remote Sens.* 1–8,  
334 <https://link.springer.com/article/10.1007/s12524-016-0649-3>.

335 Roussel, G., Ceamanos, X., Briottet, X., 2016. A sun/shadow approach for the  
336 classification of hyperspectral data. 16th Onera-DLR Aerospace Symposium  
337 (ODAS 2016), 1-7, <https://hal.archives-ouvertes.fr/hal-01385498>.

338 Sakamoto, Y., Sugimura, N., Fukuda, K., Kuwahara, T., Yoshida, K., Kurihara, J.,

339 Fukuhara, T., Takahashi, Y., 2015. Development and flight results of  
340 microsatellite bus system for RISING-2. *Trans. Jpn. Soc. Aeronaut. Space*  
341 *Sci., Aerospace Technol. Jpn.* 14 (30), 89–96.

342 Schmidt, K.S., Skidmore, A.K., 2003. Spectral discrimination of vegetation types  
343 in a coastal wetland. *Remote Sensing of Environment* 85 (1), 92–108.

344 Shaw, G.A., Burke, H.K., 2003. Spectral imaging for remote sensing. *Lincoln Lab.*  
345 *J.* 14 (1), 3–28.

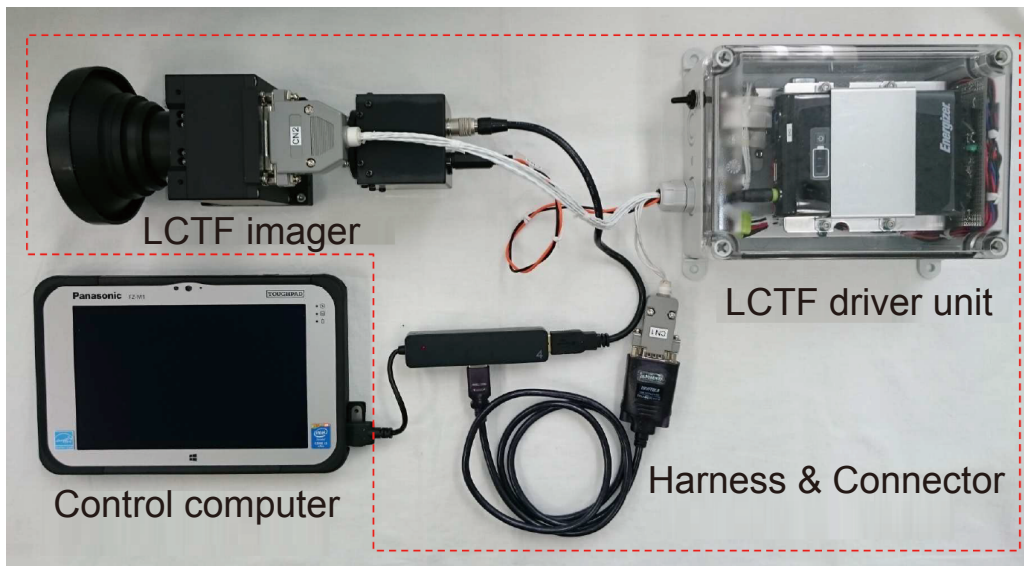
346 Singh, A., Ganapathysubramanian, B., Singh, A.K., Sarkar, S., 2016. Machine  
347 learning for high-throughput stress phenotyping in plants. *Trends Plant Sci.*  
348 21 (2), 110–124.

349 Suomalainen, J., Anders, N., Iqbal, S., Roerink, G., Franke, J., Wenting, P.,  
350 Hänniger, D., Bartholomeus, H., Becker, R., Kooistra, L., 2014. A lightweight  
351 hyperspectral mapping system and photogrammetric processing chain for  
352 unmanned aerial vehicles. *Remote Sens.* 6 (11), 11013–11030.

353 Zhang, L., Xuejian, S., Wu, T., Zhang, H., 2015. An analysis of shadow effects on  
354 spectral vegetation indexes using a ground-based imaging spectrometer.  
355 *IEEE Geosci. Remote Sens. Lett.* 12 (11), 2188–2192.

356

(a)



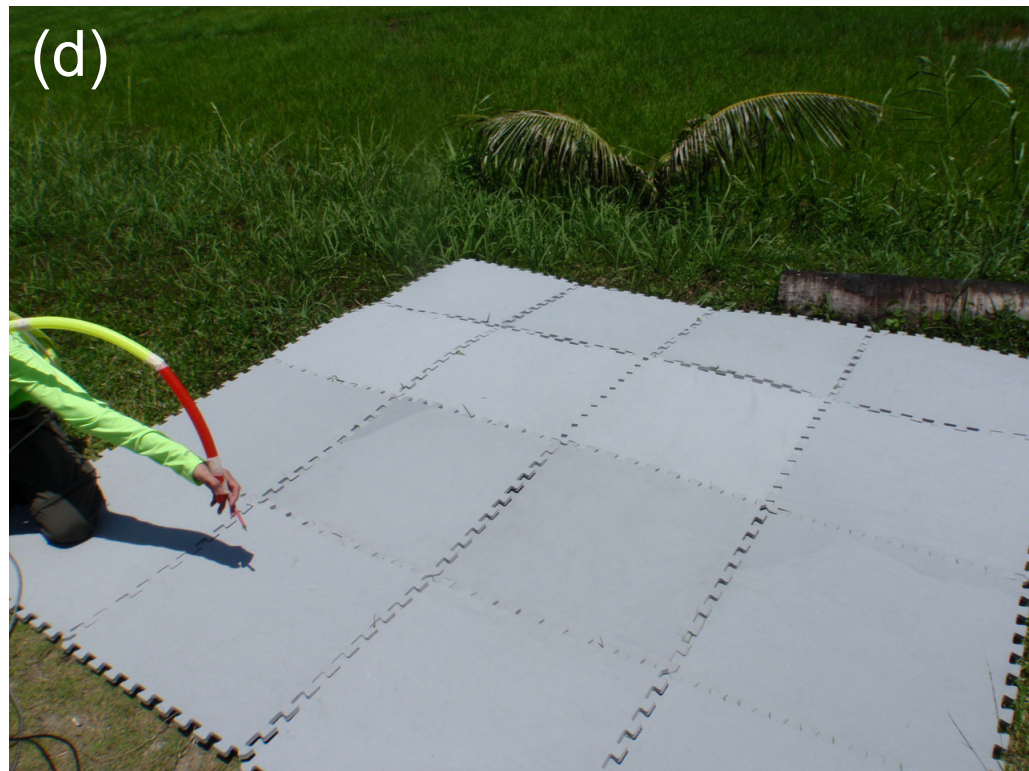
(b)

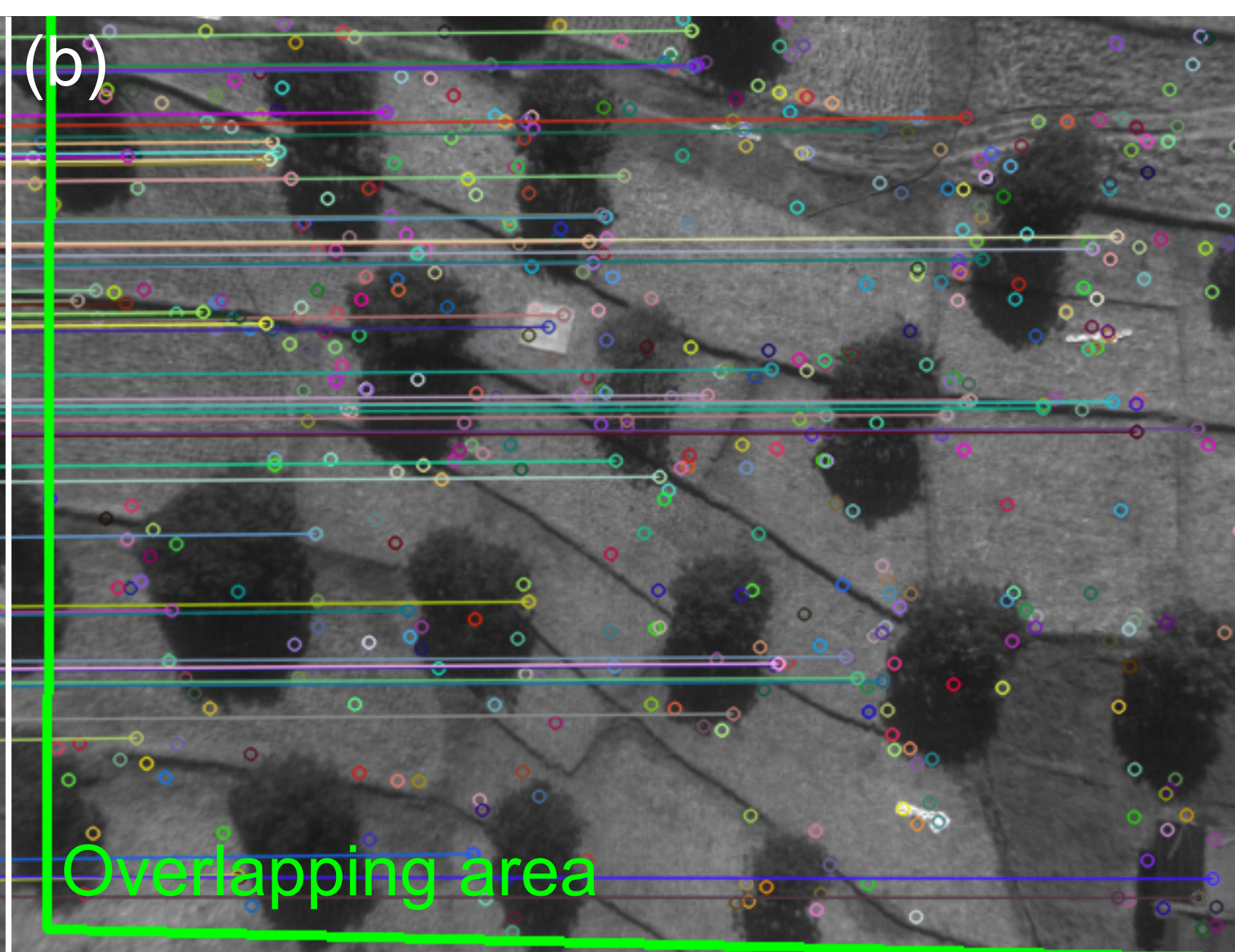
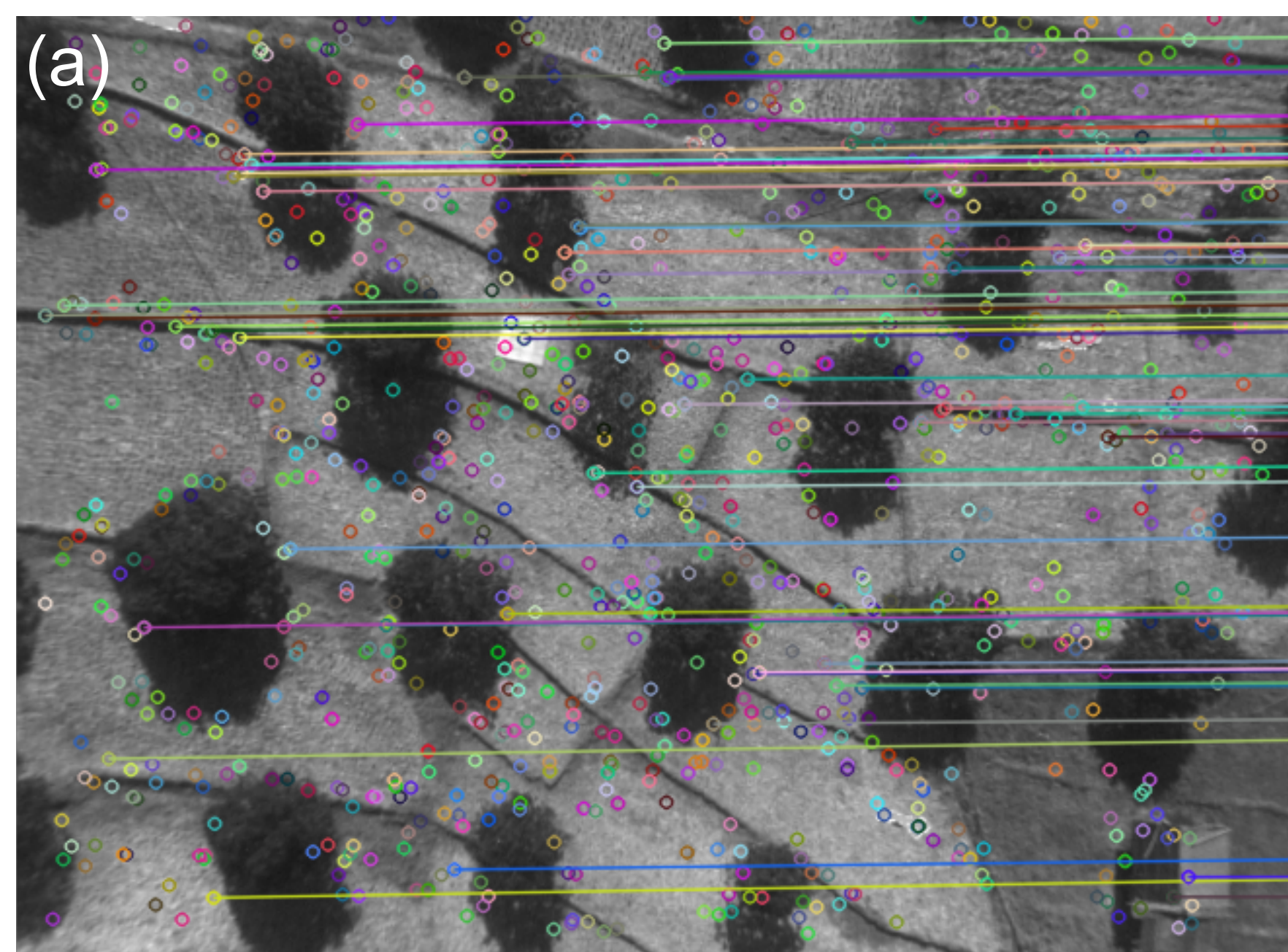


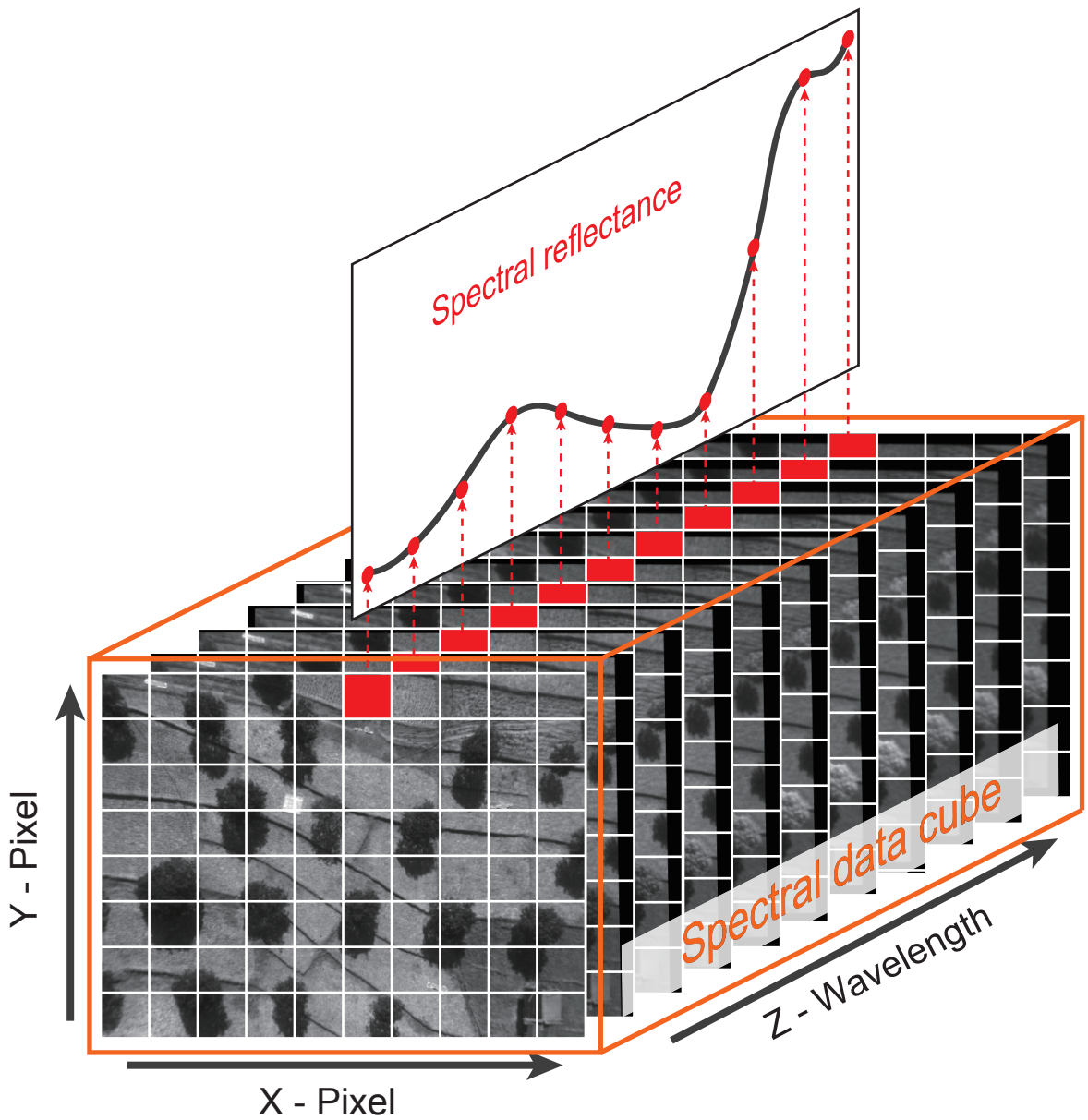
(c)

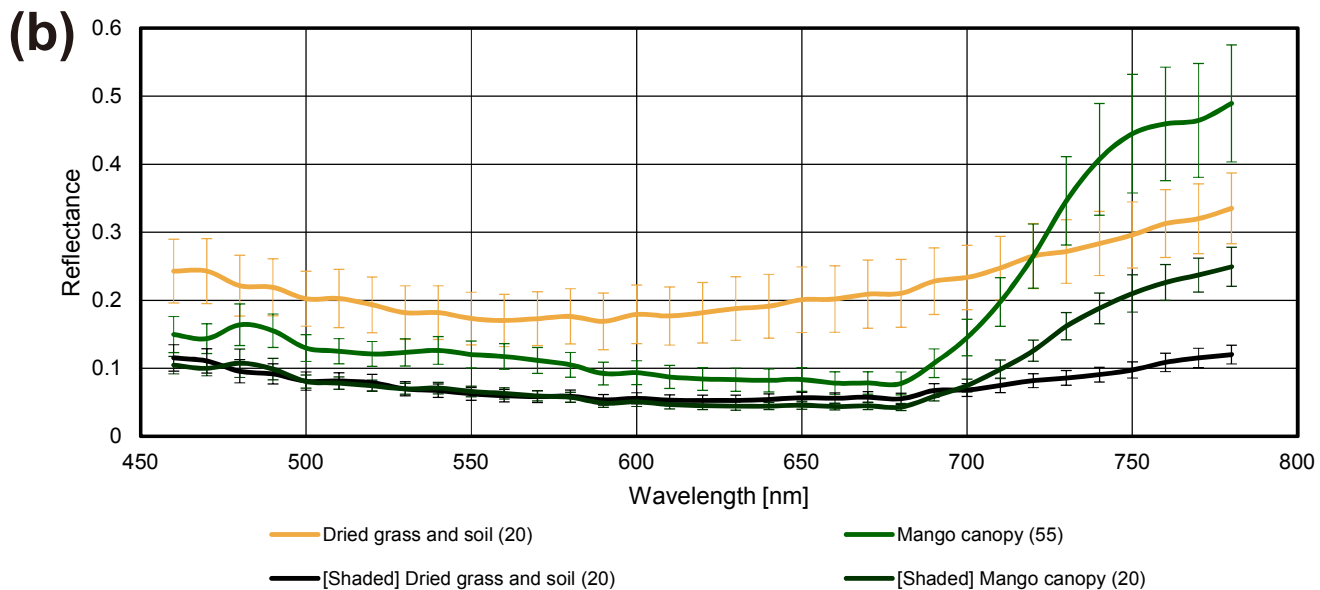
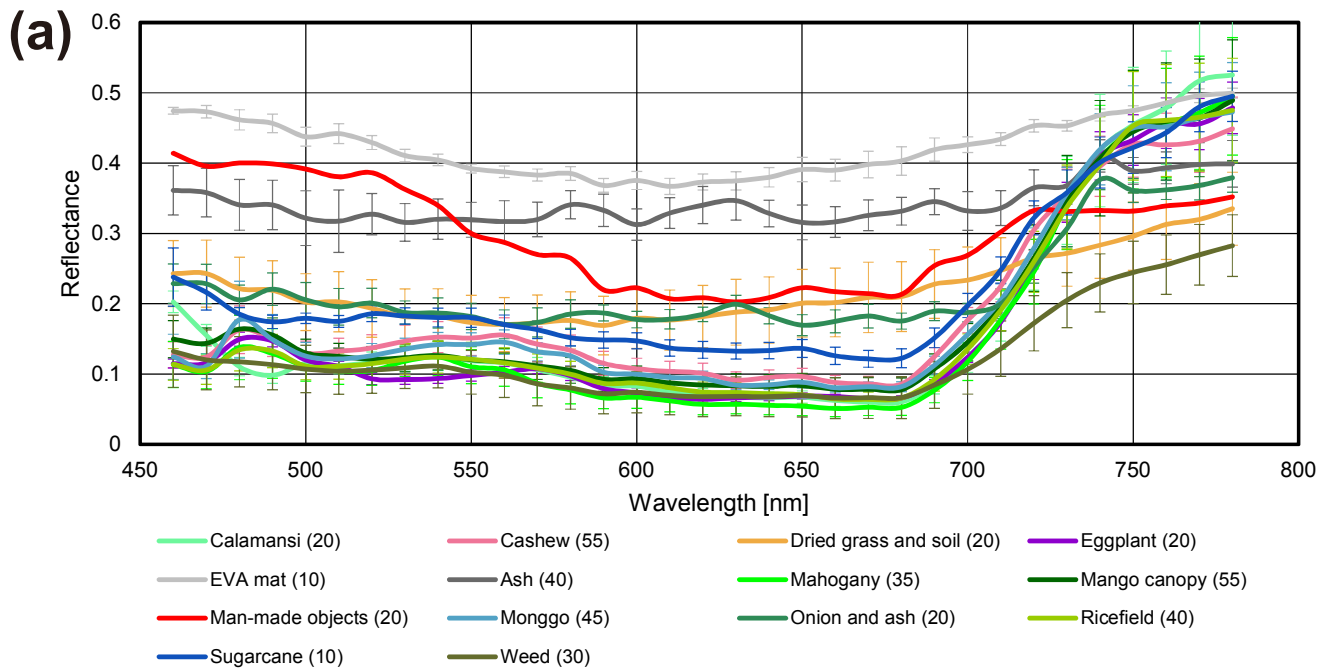


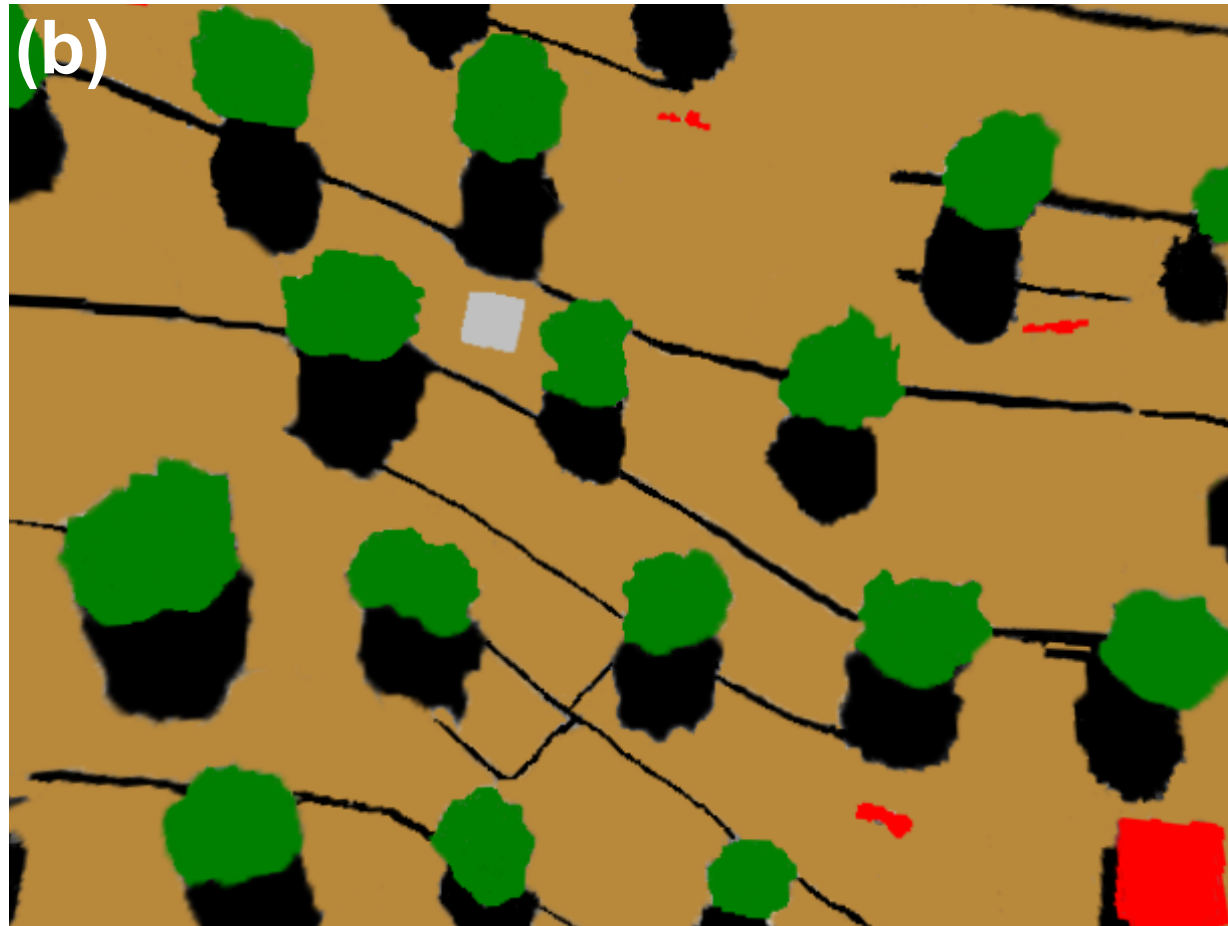
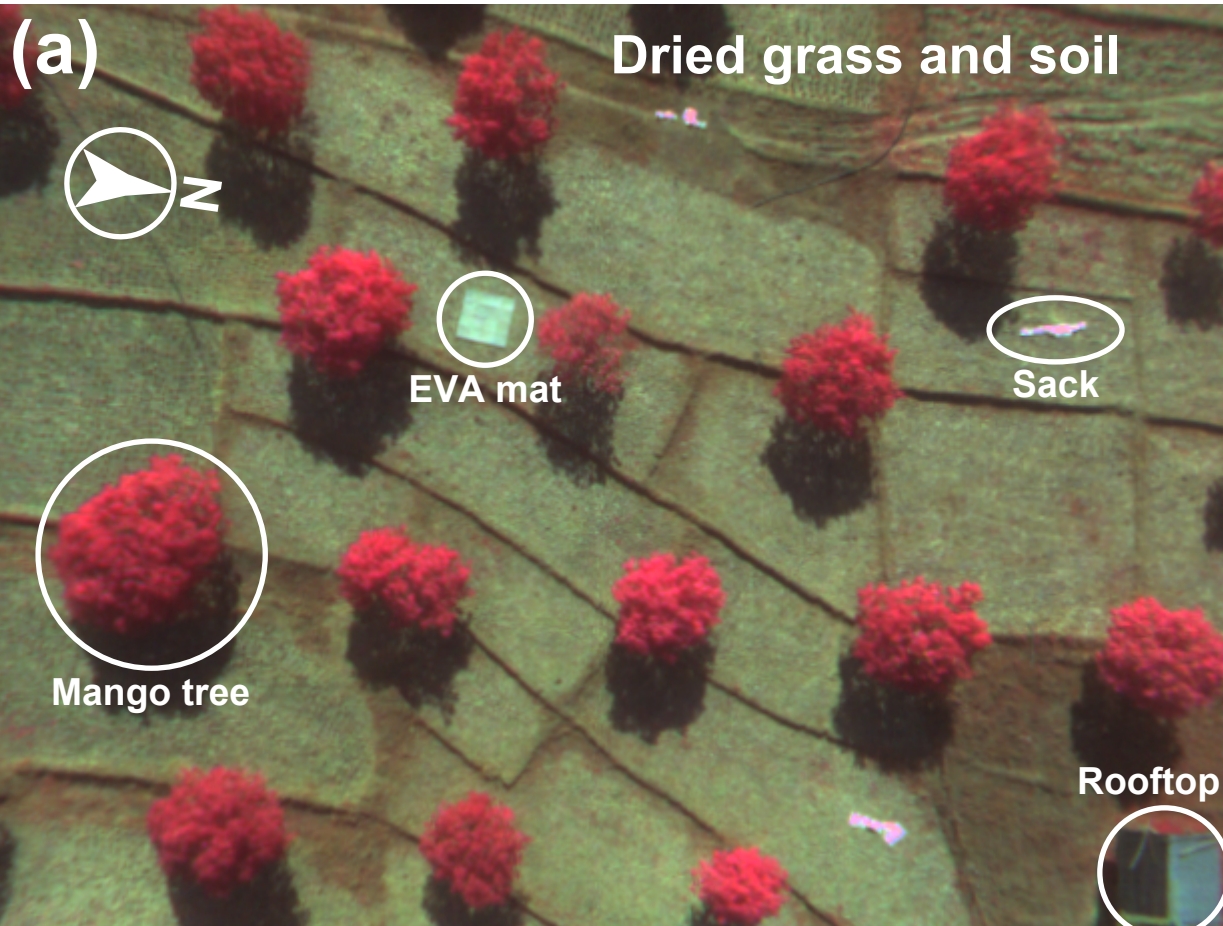
(d)

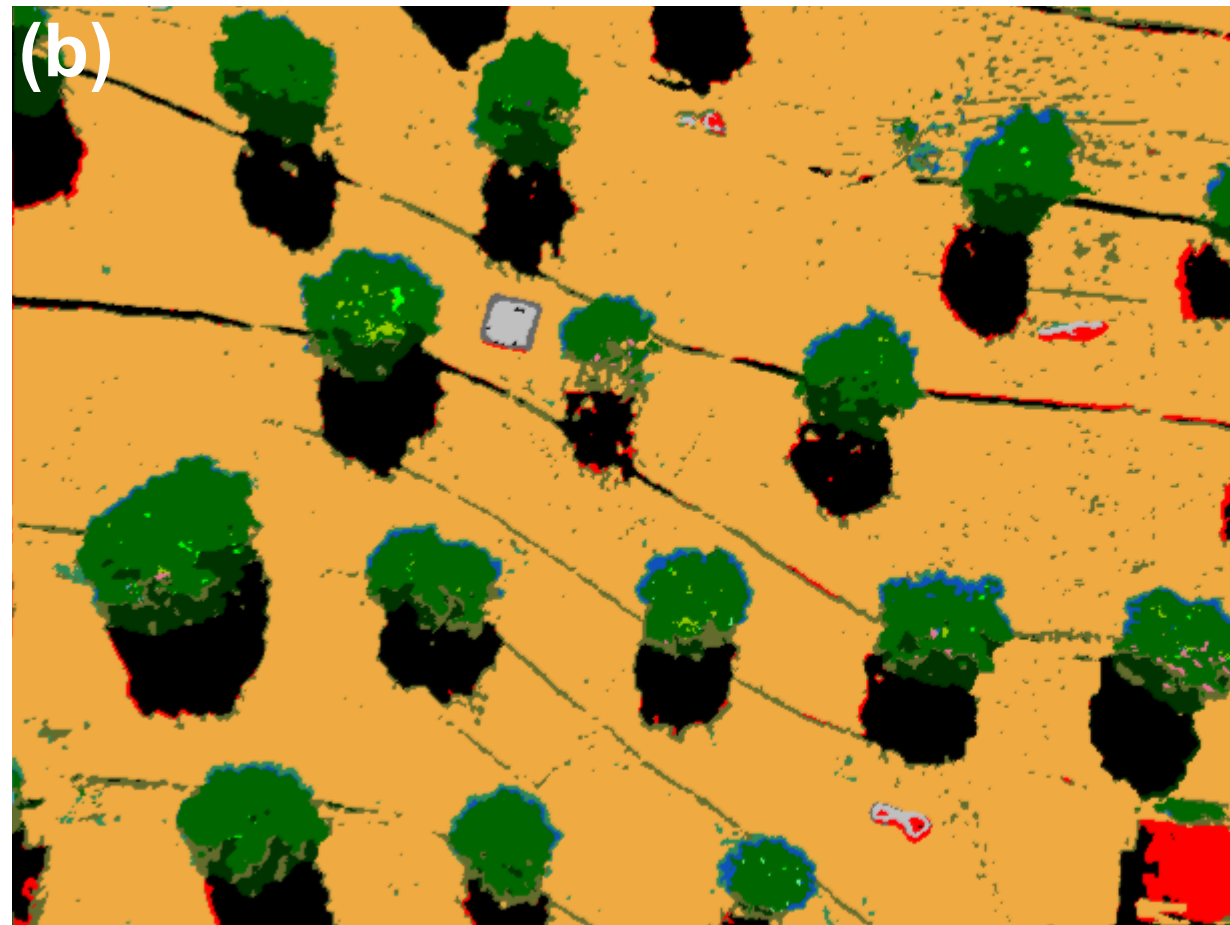
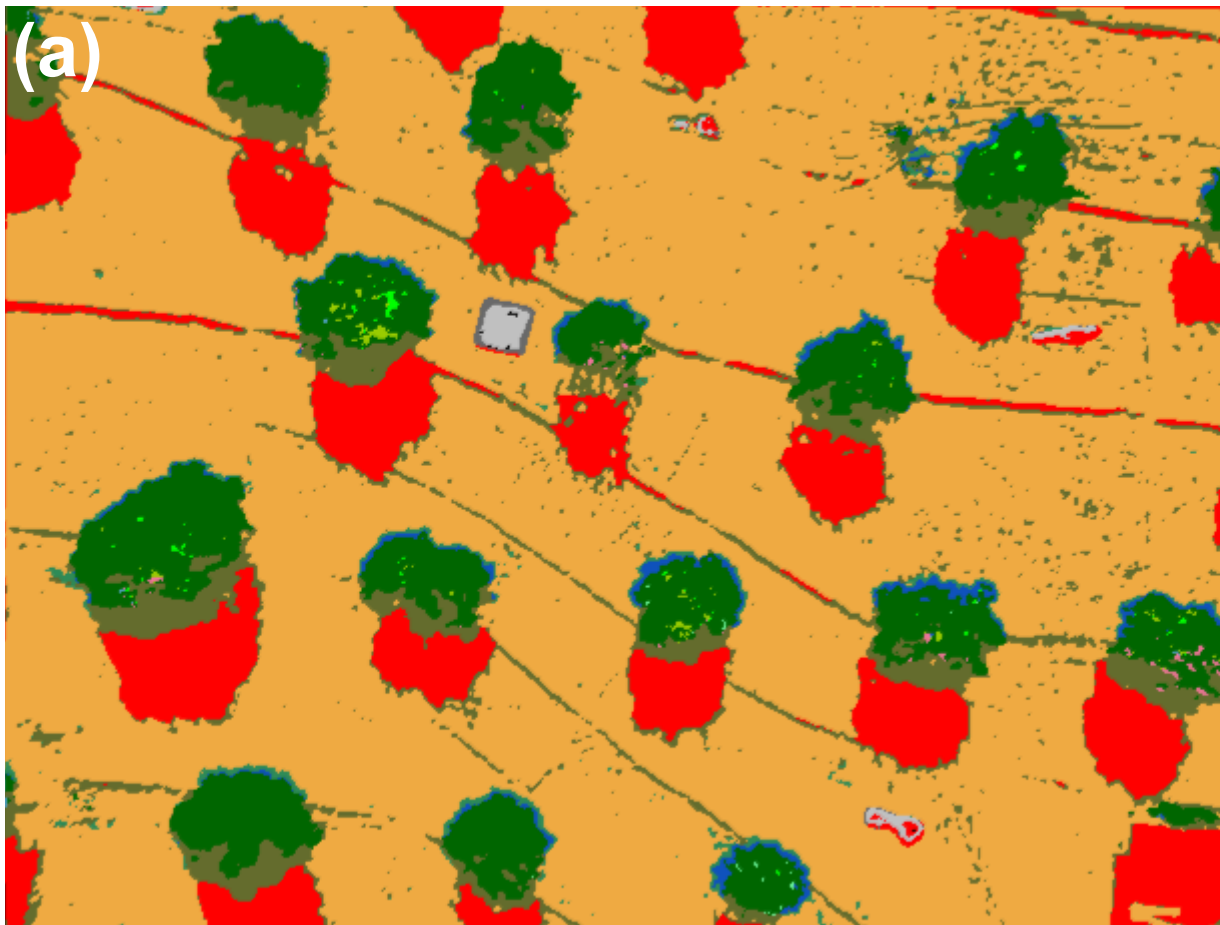












## SVM training data

### Sunlit spectra (420)

■ Calamansi (20)

■ EVA mat (10)

■ Man-made objects (20)

■ Sugarcane (10)

■ Cashew (55)

■ Ash (40)

■ Monggo (45)

■ Weed (30)

■ Dried grass and soil (20)

■ Mahogany (35)

■ Onion and ash (20)

■ Eggplant (20)

■ Mango canopy (55)

■ Ricefield (40)

### Shaded spectra (40)

■ Dried grass and soil (20)

■ Mango canopy (20)